

Article

# Structure and Properties of Protective Coatings Deposited by Pulsed Cathodic Arc Evaporation in Ar, N<sub>2</sub>, and C<sub>2</sub>H<sub>4</sub> Environments using the TiC–NiCr–Eu<sub>2</sub>O<sub>3</sub> Cathode

Philipp Kiryukhantsev-Korneev \*, Alina Sytchenko, Alexander Sheveyko and Stepan Vorotilo

Scientific-educational Center of SHS, National University of Science and Technology “MISIS”, 119049 Moscow, Russia; alina-sytchenko@yandex.ru (A.S.); sheveyko@mail.ru (A.S.); stepan.vorotylo@gmail.com (S.V.)

\* Correspondence: kiruhancev-korneev@yandex.ru; Tel.: +7-(495)-638-46-59

Received: 27 February 2019; Accepted: 26 March 2019; Published: 31 March 2019



**Abstract:** Coatings were deposited by pulsed cathodic arc evaporation (PCAE) of a TiC–NiCr–Eu<sub>2</sub>O<sub>3</sub> cathode fabricated by the powder metallurgy method. The deposition was carried out in different gas media, including Ar, N<sub>2</sub>, and C<sub>2</sub>H<sub>4</sub>. The structure, elemental, and phase compositions of coatings were studied by scanning electron microscopy (SEM), X-ray diffraction (XRD), energy-dispersive spectroscopy (EDS), Raman spectroscopy, and glow discharge optical emission spectroscopy (GDOES). Coatings were tested in terms of their hardness, elastic modulus, elastic recovery, friction coefficient, and wear and corrosion resistance. The obtained results demonstrated that the coatings deposited in Ar possessed higher hardness up to 20 GPa and an elastic recovery of 92%. Coatings produced using C<sub>2</sub>H<sub>4</sub> showed the minimum friction coefficient (0.35 ± 0.01). The use of nitrogen as a gas medium led to the formation of coatings with the best corrosion resistance in sulfuric acid. Coatings formed in N<sub>2</sub> had a free corrosion potential of +0.28 V and a corrosion current density of 0.012 μA/cm<sup>2</sup>.

**Keywords:** pulsed cathodic arc evaporation; TiC-based coatings; structure; hardness; friction coefficient; corrosion resistance

## 1. Introduction

The development of materials based on tungsten-free TiC–Ni hard alloys is a popular trend in the field of protective coatings with high wear, oxidation, and corrosion resistance [1–11]. TiC–Ni ceramic coatings are used to modify the surface of metallic materials that are used as cutting and forming tools, electrical sliding contacts, and vehicle components. In these materials, the carbide grains provide high hardness and wear resistance, whereas the nickel matrix ensures high strength and resistance against corrosion [12–15]. The additional introduction of chromium into the metallic binders enhances the mechanical properties by 2%–5% and the corrosion resistance by 80% [16], while also increasing the resistance against oxidation [17,18]. Alloying of the TiC–Ni and TiC–NiCr coatings by Si<sub>3</sub>N<sub>4</sub>, NbC, Al<sub>2</sub>O<sub>3</sub>, and ZrO<sub>2</sub> refractory compounds decreases the friction coefficient by 40% and increases the hardness and heat resistance by 30% and 25%, respectively, while also accelerating the growth of coatings [11]. The addition of ceramic nanoparticles to the cathode materials modifies the structure of the cathodes and increases their mechanical properties such as hardness (by 20%) and fracture toughness (by 40%) [19], which is essential for the increase of the cathode’s lifespan. The alloying of TiC-based coatings by rare-earth metals or metal oxides allows the modification of the coating’s structure, a decrease of the friction coefficient, and the enhancement of the coating’s mechanical properties [20,21]. In our previous investigations of electro-spark deposition using the TiC–NiCr–Eu<sub>2</sub>O<sub>3</sub> cathode, we revealed that the addition of Eu<sub>2</sub>O<sub>3</sub> provided a positive influence on the

electrical gas discharge characteristics (increasing the working pulse duration, total energy, average energy, and number of pulses), productivity of deposition [22], tribological properties, and oxidation and corrosion resistance of coatings [23].

TiC–Ni-based coatings can be manufactured by various techniques such as arc [1], laser [2] and plasma [3,4] cladding, plasma and high-velocity oxygen fuel spraying [5], electrodeposition [6], magnetron sputtering [7–10], and electro-spark deposition [11]. Cathodic arc evaporation is a prospective method for the deposition of coatings [24–26]. Due to the high energy of the deposited particles (10–100 eV), high hardness [27,28] and record-high adhesion can be attained [29,30]. Reactive cathodic arc evaporation has been successfully implemented in various environments such as N<sub>2</sub> and CH<sub>x</sub>, yielding coatings with enhanced mechanical and tribological characteristics [31–33]. The drawbacks of the method, such as the deposition of droplets and the rapid degradation of ceramic cathodes, might be partially or fully alleviated by the application of the pulsed cathodic arc evaporation (PCAE) technique [26,34–36]. In the pulsed power supply mode, the thermal stress and the high-temperature gradients on the cathode, as well as overheating of the substrate are minimized [35,36]. Currently, there is no published data regarding the deposition of TiC–Ni-based coating by cathodic arc evaporation.

The aim of this work was to investigate the coatings produced by pulsed cathodic arc evaporation using previously produced TiC–NiCr–Eu<sub>2</sub>O<sub>3</sub> cathodes.

## 2. Materials and Methods

In this work, we used a 10 × 10 × 75 mm<sup>3</sup> TiC–NiCr–Eu<sub>2</sub>O<sub>3</sub> cathode, produced by the powder metallurgy route from a mixture of titanium carbide, nickel, chromium, and europium oxide powders (81.0% TiC, 5.1% Ni, 8.2% Cr, and 5.7% Eu<sub>2</sub>O<sub>3</sub>). A detailed description of the methodology for cathode production is given elsewhere [23]. Our studies revealed that the introduction of a Eu<sub>2</sub>O<sub>3</sub> additive led to an increase in the mechanical properties of the cathode by 20% and noticeably increased its service life. Discs made of 40 Ch steel (analog—steel 5140), size Ø of 30 × 5 mm<sup>2</sup> (for tribological study), and monocrystalline silicon wafers with the (111) orientation and 20 × 20 × 0.5 mm<sup>3</sup> size (for structure investigation, mechanical, and corrosion tests) were used as the substrates. A device made on the basis of a UVM-2M vacuum system equipped with a custom evaporator (NUST MISIS, Moscow, Russia) (Figure 1) was used for the coating deposition.

The cathode is fastened in the evaporator holder by a collet. The holder itself is fastened to the PTFE tube, which acts as a load-bearing isolator to prevent the insulation breakdown. The whole construction was placed in a quartz tube. Ignition was performed using a metallic wire separated from the cathode by an alumina plate. Anode construction is based on the water-cooled magnetron. The substrate is fastened on a circular holder and is located between the cathode and the anode at a distance of 20 mm from the cathode. The working gas pressure was 0.4 Pa and the residual pressure was 4 × 10<sup>−3</sup> Pa. Ar (99.9995%), N<sub>2</sub> (99.999%), and C<sub>2</sub>H<sub>4</sub> (99.95%) were used as the deposition environments. Voltage and ignition frequencies were 15 kV and 10 Hz, respectively. The discharge voltage oscillated in the diapason of 160–200 V. Coatings were deposited without additional substrate heating. During deposition, the substrates had a floating potential. Before deposition, substrates were ultrasonically cleaned in isopropyl alcohol for 3 min and purified in vacuum with the applied 2 kV negative bias voltage for 5 min. The deposition time of coatings was 10 min for all types of substrates.

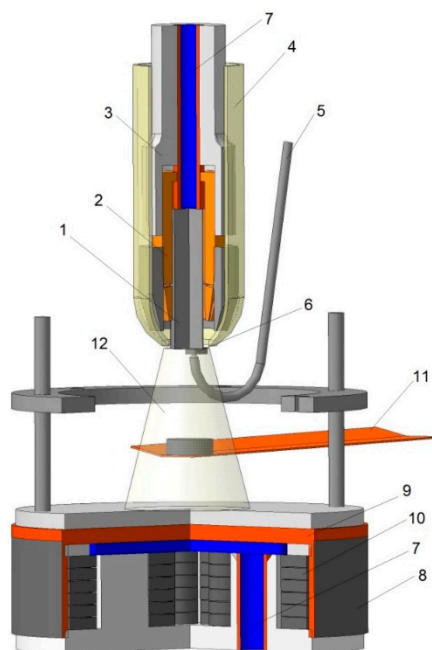


**Figure 1.** A schematic of the pulsed cathodic arc evaporation (PCA) method: 1—cathode being evaporated; 2—cathode holder; 3—isolator; 4—quartz tube; 5—ignition system; 6—ceramic; 7—water cooling system; 8—anode case; 9—copper plate; 10—magnet system; 11—substrate holder with a substrate; and 12—coating deposition zone.

Elemental distribution profiles of the coatings were obtained using a glow-discharge optical emission spectrometer (GDOES) PROFILER-2 (Horiba Jobin Yvon, Longjumeau, France). Structural analysis was performed using a Hitachi S-3400N scanning electron microscope (SEM, Tokyo, Japan), equipped with the energy-dispersive spectroscopy (EDS) add-on NORAN 7 system. The X-ray diffraction (XRD) study was performed with a D8 ADVANCE (Bruker, Mannheim, Germany) diffractometer with Cu K $\alpha$  radiation. Raman spectroscopy was performed with an NTEGRA (NT-MDT, Moscow, Russia) installation equipped with a red laser (633 nm wavelength). Hardness ( $H$ ), elastic modulus ( $E$ ), and elastic recovery ( $W$ ) were measured using a Nanohardness Tester (CSM Instruments, Peseux, Switzerland) equipped with a Berkovich indenter. The indentation load was 1 mN. Indentation curves were analyzed using the Oliver–Pharr method [37]. Tribological tests were carried out on an automated friction machine Tribometer (CSM Instruments) using the “pin-on-disc” scheme; 6 mm balls made of 400 C steel or alumina were used as the indenters where the normal load was 1 N and the linear velocity was 10 cm/s. Fractographical investigation of the wear tracks with the subsequent calculation of normalized wear rate was carried out using the Veeco WYKO NT1100 profilometer (Plainview, NY, USA). For the corrosion resistance experiments, we used the coatings deposited on the monocrystalline silicon wafers. Electrochemical investigations were performed using the three-electrode node with the “Voltalab PST050” potentiostat (Radiometer Analytical, Lyon, France) in 1 N H<sub>2</sub>SO<sub>4</sub> solution at 25 °C. All potentials were processed and correlated to the standard hydrogen reference electrode. Free corrosion potentials were measured as a function of time for 0.5 h until a stationary state was reached. Corrosion currents were calculated using the technique based on the graphical representation of the Tafel equation. The interception points of the tangents of the polarization curves were defined, and their projection on the ordinate axis was used to estimate the free corrosion current.

### 3. Results

Table 1 provides the compositions (measured by EDS) of coatings deposited using the TiC–NiCr–Eu<sub>2</sub>O<sub>3</sub> cathode in Ar, C<sub>2</sub>H<sub>4</sub>, and N<sub>2</sub>.

**Table 1.** Elemental composition of coatings and the cathode.

Coatings	Environment	Content, at. %					
		C	Ti	Cr	Ni	Eu	N
1	Ar	52.9	39.7	4.0	2.9	0.5	0
2	C <sub>2</sub> H <sub>4</sub>	86.8	10.9	1.6	0.8	0	0
3	N <sub>2</sub>	23.2	18.4	3.2	1.5	0.4	53.2
Cathode	–	45.6	45.7	5.3	2.9	0.4	0

Coating 1, deposited in Ar, had the lowest Ti content (39.7 at.%) and an over-stoichiometric surplus of C (13.2 at.%). The summarized content of Cr, Ni, and Eu was 7.4 at.%. Coating 2 had the highest carbon content (86.8 at.%) due to the additional deposition of C atoms from the C<sub>2</sub>H<sub>4</sub> environment. The presence of surplus carbon led to the formation of sp<sup>2</sup>–sp<sup>3</sup> bound carbon phases in addition to the titanium carbide. Coating 2 was characterized by a reduced content of metallic elements. In this case, the europium concentration was below the analysis threshold (0.1 at.%). In the case of deposition in the N<sub>2</sub> environment, the carbon content was decreased as compared to the non-reactive sputtered coating 1 and was equal to 23.2 at.% while the nitrogen content was 53.2 at.%, leading to the formation of the titanium carbonitride phase. A GDOES analysis of the coating deposited on the steel substrate revealed a uniform distribution of all elements. The oxygen concentration was 5.5 ± 0.5 at.% (coating 1), 3.9 ± 0.3 at.% (coating 2), and 4.6 ± 0.4 at.% (coating 3). The impurities of oxygen in the coating were due to the porosity of the cathode and the gas environment. Deviation in the content of the metal elements measured by GDOES and EDS did not exceed 20%. According to the GDOES profiles and SEM images, the coating deposited in Ar had a deposition rate of 65 nm/min, whereas the coatings deposited in C<sub>2</sub>H<sub>4</sub> or N<sub>2</sub> showed 50 nm/min.

Figure 2 provides the typical SEM images of the surface and a cross-sectional fracture of the coatings.

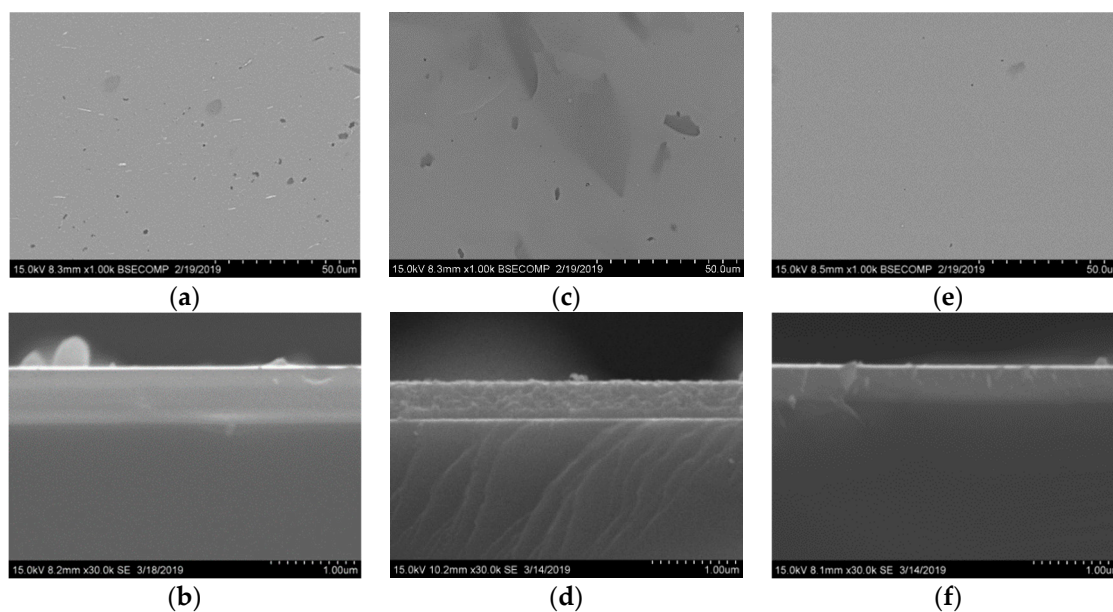


**Figure 2.** Typical plane-view and cross-sectional scanning electron microscopy (SEM) images of coatings 1 (a,b), 2 (c,d), and 3 (e,f) deposited onto the silicon.

Areas of cohesive destruction were present on the surface of coatings deposited on steel substrates in Ar and N<sub>2</sub> and occupied about 30% of the surface. The surface of the coating deposited in C<sub>2</sub>H<sub>4</sub> was less defective—the cohesion destruction areas occupied less than 2% of the surface. Deposition of coatings 1–3 onto silicon wafers resulted in higher-quality coatings (Figure 2). The structural defects

might be caused by the high level of internal stress, which influences the adhesion and cohesion strength of the coatings [38].

Figure 3 provides the XRD patterns for the coatings deposited on the silicon wafers.

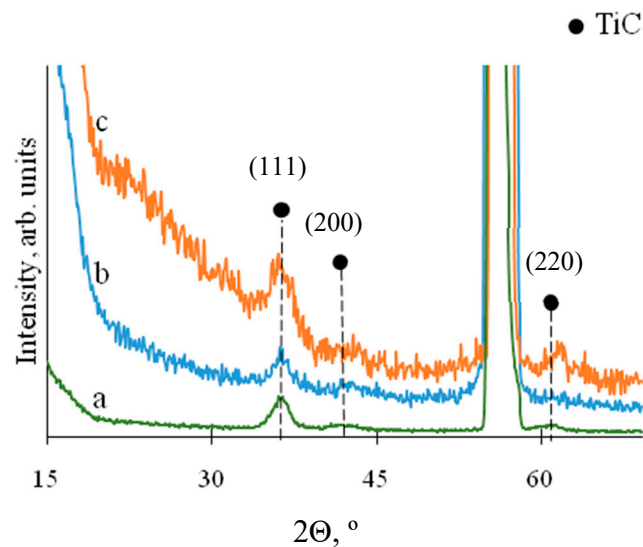


**Figure 3.** X-ray diffraction (XRD) patterns of coatings produced in Ar (a), C<sub>2</sub>H<sub>4</sub> (b), and N<sub>2</sub> (c).

A sharp and intense peak at  $2\theta = 55.3^\circ$ , present on all the XRD patterns, belongs to silicon. All coatings featured the peaks corresponding to (111), (200), and (220) planes of the TiC-based FCC phase. The presence of the (111) preferential orientation in coatings compared to the standard TiC powders is noticeable. The crystallite size of TiC, calculated from the broadening of (200) and (220) peaks using the Scherer's formula, was 4.5–8.1 nm and did not depend on the gas environment. However, a similar analysis of the (111) peak revealed that the TiC crystallite size was 4.4, 5.8, and 7.3 nm for the coatings deposited in Ar, N<sub>2</sub>, and C<sub>2</sub>H<sub>4</sub>, respectively. The lattice parameter appeared to be the same (within the error boundaries of  $\pm 0.001$  nm) for all coatings. A calculation on the basis of the (111), (200), and (220) peaks showed corresponding values of 0.430, 0.424, and 0.425 nm. The deviation of the lattice parameter from the table value ( $a = 0.432$  nm [39]) might be related to the presence of minor admixtures of Ni, Cr, Eu, and O in the TiC crystal lattice [40].

Raman spectra of TiC–NiCr–Eu<sub>2</sub>O<sub>3</sub> coatings deposited in Ar, C<sub>2</sub>H<sub>4</sub>, and N<sub>2</sub> are provided in Figure 4.

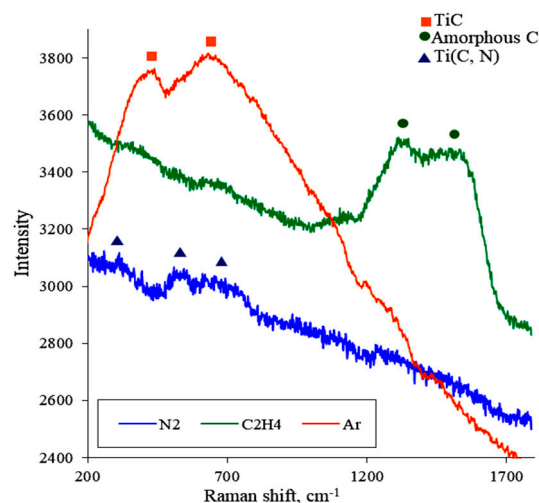


**Figure 4.** Raman spectra of the coatings.

The coating deposited in Ar had peaks located at 430 and 655  $\text{cm}^{-1}$ , which corresponded to the TiC phase [41]. The coating deposited in  $\text{N}_2$  had peaks at 300, 520, and 690  $\text{cm}^{-1}$ . This shift towards lower frequencies and the decrease in peak intensities was caused by the partial substitution of C atoms by N in the TiC lattice and formation of the TiCN phase [42]. Raman spectrum of the coating deposited in  $\text{C}_2\text{H}_4$  contained additional peaks at 1340 and 1500  $\text{cm}^{-1}$ , whose position and form corresponded to amorphous carbon [43]. In this case, the intensity of TiC peaks was substantially reduced, as the main fraction of all chemical bonds in this coating corresponded to C–C bonds. None of the Raman spectra featured the europium oxide peak at 338  $\text{cm}^{-1}$  [44], probably due to the low concentrations of  $\text{Eu}_2\text{O}_3$  in coatings.

Table 2 provides the mechanical properties of coatings on steel substrates measured by nanoindentation.

**Table 2.** Mechanical properties of coatings.

Coating	Environment	$H$ , GPa	$E$ , GPa	$W$ , %	$H/E$	$H^3/E^2$ , GPa
1	Ar	20.2	166	92	0.12	0.30
2	$\text{C}_2\text{H}_4$	17.0	191	84	0.09	0.13
3	$\text{N}_2$	16.5	152	90	0.11	0.19

The coating deposited in Ar had the highest hardness ( $H = 20.2$  GPa) and outstanding elastic recovery ( $W = 92\%$ ). Such high value can be explained by the high sensitivity of the  $W$  parameter to the depth of the indentation. Indeed, repeated experiments by nanoindentation at a higher load of 4 mN gave a value of 68% for coating 1. The transition to reactive evaporation decreased both the value of  $H$  by 15%–18% and the value of  $W$  by 2%–9%.

Tribological testing of coatings was performed using the balls made of 440 C steel or  $\text{Al}_2\text{O}_3$ . When the steel ball was used as the counter-body, coating 1 was characterized by the lowest friction coefficient of 0.22, which remained constant during the whole wear distance (Figure 5).

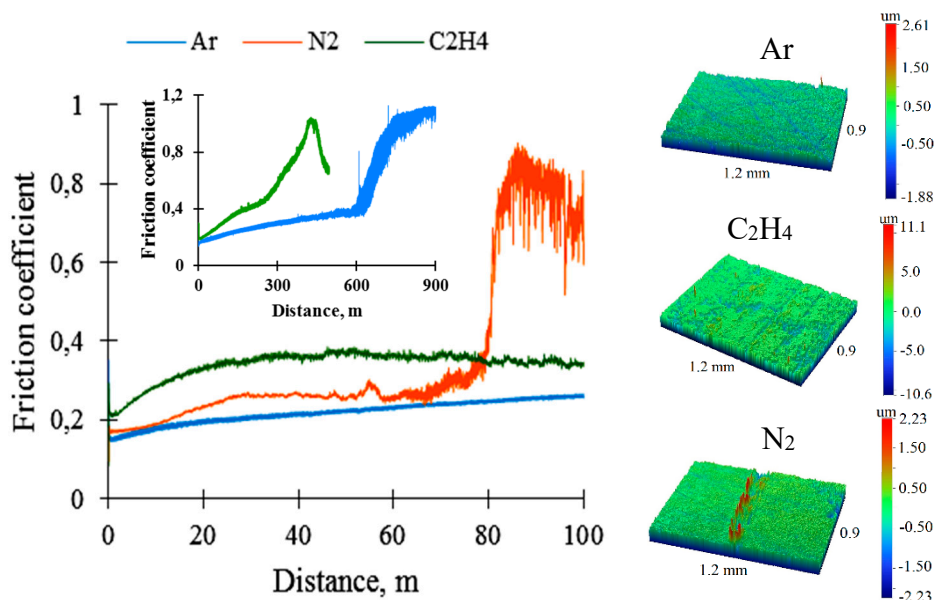


**Figure 5.** Dependence of the friction coefficient on the distance and 3D profiles of tribo-contact zones (440 C steel counter-body). The figure insert shows the results at a higher distance for coatings 1 and 2.

In the case of coating 2 deposited in  $\text{C}_2\text{H}_4$ , the friction coefficient increased gradually up to 20 m distance and then slowly decreased. The median value for the friction coefficient was 0.34. In the case of coating 3, the friction coefficient rose steadily during the first 80 m distance, and then increased

dramatically up to  $\sim 0.8$  due to the complete wear of the coating. Coatings 1 and 2 deposited in Ar and  $C_2H_4$  were able to withstand the wear over the full 100 m distance. Optical profilometry of the wear tracks revealed that the wear depth for coatings 1 and 2 was insignificant and comparable with the roughness of the initial coatings. Therefore, the wear rate could not be calculated (Figure 5). However, clear wear tracks were discernible on the tribo-contact zone of coating 3. Therefore, the coatings deposited in argon and ethylene demonstrated the highest wear resistance against the steel ball. An additional study was performed to reveal the best coating with the maximal wear resistance (Figure 5, insert). At a distance of 600 m, the friction coefficient of the coating 1 monotone increased from 0.19 to 0.36, after which there was a kink that was associated with the beginning of the destruction of the coating. A further increase in the friction coefficient was associated with the complete wearing of the coating and the formation of a metal–metal contact (ball–substrate), which was characterized by a high value of the friction coefficient close to 1. The friction coefficient of coating 2 monotonically increased from 0.23 to 0.44 at a distance ranging from 0 to 250 m. Intensive failure of the coating occurred between 250 and 450 m. The decrease in the friction coefficient after 450 m could be explained by the lubricating effect of the wear products with a high volume of  $sp^2$ – $sp^3$  carbon particles (debris). Thus, coating 1 demonstrated the maximal wear resistance.

Figure 6 reveals the dependence of the friction coefficient on the distance along with the 3D profiles of the tribo-contact zones, formed by an  $Al_2O_3$  ball.

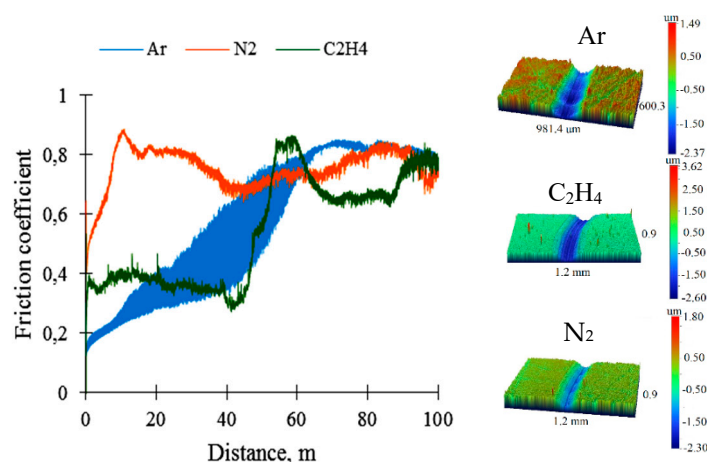


**Figure 6.** Dependence of the friction coefficient on the distance and 3D profiles of the tribo-contact zones ( $Al_2O_3$  counter-body).

During the testing of the coating deposited in Ar, the friction coefficient increased from 0.18 to 0.8 throughout the whole distance with complete wear of the coating occurring at 60 m. The mean friction coefficient for coating 1 was 0.54. The coating deposited in  $C_2H_4$  demonstrated a stable friction coefficient of 0.36 up to 46 meters but was followed by a sharp increase due to the full wear of the coating. The coating sputtered in nitrogen had the highest initial friction coefficient of 0.5, which then increased up to  $\sim 0.87$  and oscillated in the 0.70–0.85 diapason during the rest of the test. This behavior was related to the complete wear of coating 3 during the first 10 meters of the test. The investigation of wear tracks revealed that the wear rates were  $9.2 \times 10^{-5}$ ,  $4.8 \times 10^{-5}$ , and  $5.0 \times 10^{-5} \text{ mm}^3/(\text{Nm})$  for coatings 1, 2, and 3, respectively.

The results of the electrochemical testing of coatings 1–3 deposited onto silicon are provided in Figure 7 as polarization curves, both in linear and semi-logarithmic coordinates.

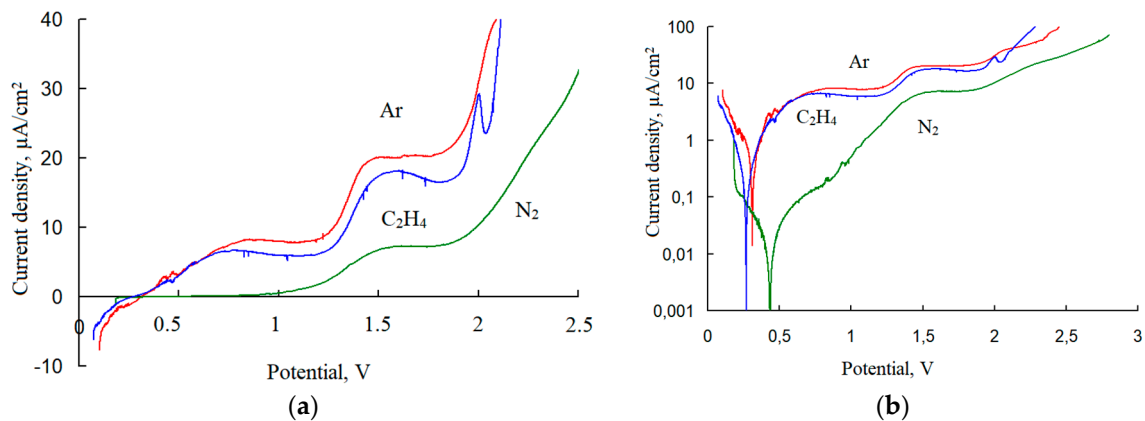


**Figure 7.** Polarization curves for the coatings in linear (a) and semi-logarithmic (b) coordinates.

The free corrosion potential  $\varphi$  and corrosion current density  $i_{\text{COR}}$  are shown in Table 3.

**Table 3.** Electrochemical properties of coatings.

Coating	Environment	$\varphi$ , V	$i_{\text{COR}}$ , $\mu\text{A}/\text{cm}^2$
1	Ar	0.30	0.45
2	C <sub>2</sub> H <sub>4</sub>	0.38	0.23
3	N <sub>2</sub>	0.28	0.012

The stable free corrosion potentials were +0.3, +0.38, and +0.28 V for the coatings deposited in Ar, C<sub>2</sub>H<sub>4</sub>, and N<sub>2</sub>, respectively. All the coatings remained passivated and stable in sulfuric acid. During the anodic polarization in the 0.5–1 V diapason, coatings deposited in argon and ethylene demonstrated an activation peak of the current density, related to the oxidation of carbides of titanium and chromium with the subsequent isolation of the surface by oxide layers. For the coating deposited in nitrogen, this peak shifted towards the 1–1.5 V potentials. At potentials above 2 V, a breakdown of passive layers occurred for all the coatings. The calculated corrosion current density was 0.45  $\mu\text{A}/\text{cm}^2$  for the coating deposited in Ar, 0.012  $\mu\text{A}/\text{cm}^2$  for the coating deposited in N<sub>2</sub>, and 0.23  $\mu\text{A}/\text{cm}^2$  for the coating deposited in C<sub>2</sub>H<sub>4</sub>. Comparison of the corrosion data revealed that the coating deposited in nitrogen was characterized by the highest corrosion resistance.

#### 4. Discussion

One of the main advantages of combined application of PCAE and Eu<sub>2</sub>O<sub>3</sub>-doped metal-ceramic electrodes was the structural uniformity of the deposited coatings. Neither the volume nor surface ( $R_a = 3\text{--}5$  nm for coatings on Si wafers with  $R_a = 0.9$  nm) of the coatings 1–3 contained the inclusions of droplet phase, which is ubiquitous in the coatings deposited by cathodic arc evaporation [45–47]. Usually, the size of the macroparticles varies from ones to dozens of microns [48]. The elimination of droplet phase is evidently caused to the combination of various factors. The first factor is the considerable decrease of the cathode overheating during the PCAE as compared to the conventional cathodic arc evaporation due to the higher number of cathodic spots and their velocity [36,49]. Another factor is the high strength of the employed cathode, which was the result of both the presence of NiCr binder and Eu<sub>2</sub>O<sub>3</sub> reinforcing particles in the cathode. Previously used binder-free ceramic electrodes (for example, chromium diboride) experienced rapid fragmentation due to spalling of ceramic phase grains in PCAE evaporator (Figure 1) and produced a significant amount of droplet particles in the coatings. Eu<sub>2</sub>O<sub>3</sub>-free TiC-NiCr cathodes had increased strength as compared to pure ceramics due to the presence of metallic binder phase. However, cathodes could not withstand local overheating and quickly failed due to cracking. TiC-NiCr-Eu<sub>2</sub>O<sub>3</sub> cathodes featured 20% higher mechanical properties as compared to their Eu<sub>2</sub>O<sub>3</sub>-free analogs and endured up to 30 deposition cycles without any noticeable

crumbling. Therefore, albeit the  $\text{Eu}_2\text{O}_3$  content in deposited coatings was negligible, this additive had a pronounced impact on the cathode performance.

In addition to the absence of droplet phase, the coatings 1–3 produced in this work did not feature columnar growth of crystallites common for the cathodic arc deposited coatings [50,51]. The columnar structure is often detrimental for the mechanical and tribological properties as well as the corrosion resistance of the coatings [29,52].

Coatings 1–3 had a relatively low elastic modulus  $E$  within the 152–191 GPa diapason, which is close to the elastic modulus of Si (170 GPa), but differs more considerably from the elastic modulus of steel (224 GPa). Accordingly, coatings deposited on Si substrate had higher cohesive/adhesive strength and quality. Deposition of the coating in carbon-containing environment ( $\text{C}_2\text{H}_4$ ) has led to a drastic improvement of the cohesive strength due to the formation of amorphous carbon phase (peaks at 1340 and 1500  $\text{cm}^{-1}$  in Raman spectra, Figure 4). Moreover, the coating deposited in  $\text{C}_2\text{H}_4$  provided the lowest friction coefficient during the tribological test performed using alumina ball as a counterbody. Friction coefficient was equal to 0.36 and remained stable until the coating was fully worn out (46 m). This feature, along with increased adhesive strength, can be attributed to the presence of amorphous carbon in the coating's microstructure. However, when the relatively soft steel ball was used for the tribological tests, the coating deposited in Ar provided the lowest friction coefficient (0.19–0.36). Amorphous carbon usually reduces the friction coefficient of the coatings, but has a moderately detrimental effect on the hardness of the coatings (Table 2). Therefore, against softer counterparts (but on long distance) the coating deposited in Ar provides superior tribological properties, whereas against harder counterparts the coating deposited in  $\text{C}_2\text{H}_4$  outperforms other specimens. The noticeable reduction of both mechanical properties and tribological performance of coating deposited in  $\text{N}_2$  can be attributed to the partial amorphization of the coating due to introduction of excess nitrogen.

The hardness of coatings exceeded the substrates hardness (4 GPa for steel and 14 for Si) by 18%–45%. Nanoindentation data was used for the calculation of  $H/E$  and  $H^3/E^2$  parameters (Table 2), which might indicate the coating's wear resistance [53] and deformation mode [54]. According to the literature data, the excessive concentration of carbon in titanium carbonitride coatings leads to a marked decrease in mechanical properties. Authors of work [55] reported that coatings with excess carbon ( $\text{Ti}/\text{C} = 0.15\text{--}0.19$ ) had relatively low mechanical properties:  $H = 7.6\text{--}10.4$  GPa,  $E = 87\text{--}109$  GPa,  $H/E = 0.09\text{--}0.10$ , and  $H^3/E^2 = 0.06\text{--}0.09$  GPa. Coatings with concentration ratio  $\text{Ti}/(\text{C}+\text{N}) = 0.61$  exhibited  $H = 17$  GPa,  $H/E = 0.059$  and  $H^3/E^2 = 0.060$  GPa [56]. TiCN coatings with lower carbon content have hardness about 22–23 GPa and elastic modulus in range 215–250 GPa [57,58].

Among the previously investigated materials, the most similar in composition Cr-doped TiCN coatings tested under similar conditions demonstrated a higher friction coefficient ( $>0.4$ ) [59]. However, the PCAE coatings investigated in this work were characterized by slightly lower corrosion resistance as compared to the previously reported magnetron-sputtered TiCN [56] and TiC-NiAl [7] coatings.

## 5. Conclusions

Coatings were deposited onto steel and silicon substrates by pulsed cathodic arc evaporation of the TiC-NiCr-Eu<sub>2</sub>O<sub>3</sub> cathode in Ar,  $\text{C}_2\text{H}_4$ , and  $\text{N}_2$  environments. The TiC-based FCC phase with a crystallite size of 4–8 nm was the main constituent of the coatings. The introduction of nitrogen led to the formation of TiCN phase, whereas the increase of carbon content led to the formation of amorphous carbon. Coatings deposited in Ar were characterized by the highest hardness of 20 GPa and a record-high elastic recovery of 92%. The substitution of argon by nitrogen or ethylene had a detrimental effect on the coating's mechanical properties.

The coating deposited in Ar, upon wearing by the steel body, demonstrated a low friction coefficient of 0.2 and a good wear resistance. When  $\text{Al}_2\text{O}_3$  was used as the counter-body, the coating showed a constant rise of friction coefficient from 0.18 to ~0.8 due to the coating's gradual destruction. Coatings with the maximum carbon content demonstrated satisfactory wear resistance and a low friction coefficient of 0.34–0.36 against both steel and  $\text{Al}_2\text{O}_3$  balls due to the formation of an  $\text{sp}^2\text{--sp}^3$

bound carbon phase. The introduction of nitrogen in the coatings led to a considerable deterioration of the coating's tribological performance.

Coatings deposited in nitrogen had the lowest free corrosion potential of +0.28 V in H<sub>2</sub>SO<sub>4</sub>. The corrosion current density decreased from 0.45 to 0.23  $\mu\text{A}/\text{cm}^2$  with the transition from non-reactive sputtering to sputtering in the C<sub>2</sub>H<sub>4</sub> environment and then to 0.012  $\mu\text{A}/\text{cm}^2$  when the N<sub>2</sub> environment was used. The produced coatings can be recommended for the protection of steel parts from mechanical wear and corrosion.

**Author Contributions:** Author Contributions: Supervision, P.K.-K.; Investigation, P.K.-K., A.S. (Alina Sytchenko), A.S. (Alexander Sheveyko); Formal Analysis, P.K.-K., A.S. (Alina Sytchenko); Writing—Original Draft Preparation, P.K.-K.; Writing—Review & Editing, P.K.-K., S.V.

**Conflicts of Interest:** The authors declare no conflict of interest.

## References

- Sahoo, C.K.; Masanta, M. Microstructure and mechanical properties of TiC–Ni coating on AISI304 steel produced by TIG cladding process. *J. Mater. Process. Technol.* **2017**, *240*, 126–137. [[CrossRef](#)]
- Wei, Q.; Pang, X.; Zhou, J.; Chen, C. High temperature spectral selective TiC–Ni/Mo cermet-based coatings for solar thermal systems by laser cladding. *Solar Energy* **2018**, *171*, 247–257. [[CrossRef](#)]
- Liu, Y.; Feng, Z.; Pu, F.; Xia, Z.; Sun, G.; Zhang, L.; Shi, C.; Zhang, Z. Microstructure and dry-sliding wear properties of TiC/CaF<sub>2</sub>/ $\gamma$ -Ni self-lubricating wear-resistant composite coating produced by co-axial powder feeding plasma transferred arc (PTA) cladding process. *Surf. Coat. Technol.* **2018**, *345*, 61–69. [[CrossRef](#)]
- Huang, S.; Sun, D.; Wang, W.; Xu, H. Microstructures and properties of in-situ TiC particles reinforced Ni-based composite coatings prepared by plasma spray welding. *Ceram. Int.* **2015**, *41*, 12202–12210. [[CrossRef](#)]
- Qi, X.; Eigen, N.; Aust, E.; Gärtner, F.; Klassen, T.; Bormann, R. Two-body abrasive wear of nano- and microcrystalline TiC–Ni-based thermal spray coatings. *Surf. Coat. Technol.* **2006**, *200*, 5037–5047. [[CrossRef](#)]
- Kartal, M.; Buyukbayram, I.; Alp, A.; Akbulut, H. Production of pulse electrodeposited Ni–TiC nanocomposite coatings. *Mater. Today Proc.* **2017**, *4*, 6982–6989. [[CrossRef](#)]
- Kiryukhantsev-Korneev, P.; Sheveyko, A.; Shvindina, N.; Levashov, E.; Shtansky, D. Comparative study of Ti–C–Ni–Al, Ti–C–Ni–Fe, and Ti–C–Ni–Al/Ti–C–Ni–Fe coatings produced by magnetron sputtering, electro-spark deposition, and a combined two-step process. *Ceram. Int.* **2018**, *44*, 7637–7646. [[CrossRef](#)]
- Grandin, M.; Nedfors, N.; Sundberg, J.; Jansson, U.; Wiklund, U. Ti–Ni–C nanocomposite coatings evaluated in a sliding electrical contact application. *Surf. Coat. Technol.* **2015**, *276*, 210–218. [[CrossRef](#)]
- André, B.; Lewin, E.; Jansson, U.; Wiklund, U. Friction and contact resistance of nanocomposite Ti–Ni–C coatings. *Wear* **2011**, *270*, 555–566. [[CrossRef](#)]
- Daniel, J.; Souček, P.; Bernátová, K.; Zábanský, L.; Stupavská, M.; Buršíková, V.; Vašina, P. Investigation of the influence of Ni doping on the structure and hardness of Ti–Ni–C coatings. *J. Nanomater.* **2017**, *2017*, 6368927. [[CrossRef](#)]
- Levashov, E.; Kudryashov, A.; Vakaev, P.; Shtansky, D.; Malochkin, O.; Gammel, F.; Suchentrunk, R.; Moore, J.; Shtansky, D. The prospects of nanodispersive powders application in surface engineering technologies. *Surf. Coat. Technol.* **2004**, *180*, 347–351. [[CrossRef](#)]
- Rajabi, A.; Ghazali, M.; Syarif, J.; Daud, A. Development and application of tool wear: A review of the characterization of TiC-based cermets with different binders. *Chem. Eng. J.* **2014**, *255*, 445–452. [[CrossRef](#)]
- Tan, Y.; He, L.; Wang, X.; Hong, X.; Wang, W. Tribological properties and wear prediction model of TiC particles reinforced Ni-base alloy composite coatings. *Trans. Nonferr. Met. Soc. China* **2014**, *24*, 2566–2573. [[CrossRef](#)]
- Zohari, S.; Sadeghian, Z.; Lotfi, B.; Broeckmann, C. Application of spark plasma sintering (SPS) for the fabrication of in situ Ni–TiC nanocomposite clad layer. *J. Alloy. Compd.* **2015**, *633*, 479–483. [[CrossRef](#)]
- Bin, C.; Tan, Y.; Long, H.; Hua, T.; Li, G. Tribological properties of TiC particles reinforced Ni-based alloy composite coatings. *Trans. Nonferr. Met. Soc. China* **2013**, *23*, 1681–1688.
- Chen, S.; Xiong, W.; Yao, Z.; Zhang, G.; Chen, X.; Huang, B.; Yang, Q. Corrosion behavior of Ti(C,N)–Ni/Cr cermets in H<sub>2</sub>SO<sub>4</sub> solution. *Int. J. Refract. Met. Hard Mater.* **2014**, *47*, 139–144. [[CrossRef](#)]

17. Wang, D.; Wang, W.; Chen, X.; Chi, C.; Wang, M.; Han, X.; Xie, Y. Influence of Cr addition on the interface purification of vacuum brazed NiCr–Cr<sub>3</sub>C<sub>2</sub> coatings on single crystal superalloy. *Surf. Coat. Technol.* **2017**, *325*, 200–209. [[CrossRef](#)]
18. Solecka, M.; Radziszewska, A.; Rutkowski, B. New insight on study of Ni-base alloy clad layer after oxidation at 650 °C. *Corros. Sci.* **2019**, *149*, 244–248. [[CrossRef](#)]
19. Levashov, E.A.; Malochkin, O.V.; Kudryashov, A.E.; Gammel, F.; Suchentrunk, R. Effects of nanocrystalline powders additions on the characteristics of combustion process, phase- and structure-formation, and properties of SHS alloys on titanium carbide base. *J. Mater. Synth. Process.* **2002**, *10*, 231–236. [[CrossRef](#)]
20. Quazi, M.; Fazal, M.A.; Haseeb, A.; Yusof, F.; Masjuki, H.; Arslan, A. Effect of rare earth elements and their oxides on tribo-mechanical performance of laser claddings: A review. *J. Rare Earths* **2016**, *34*, 549–564. [[CrossRef](#)]
21. Sun, S.; Fu, H.; Ping, X.; Guo, X.; Lin, J.; Lei, Y.; Wu, W.; Zhou, J. Effect of CeO<sub>2</sub> addition on microstructure and mechanical properties of in-situ (Ti, Nb)C/Ni coating. *Surf. Coat. Technol.* **2019**, *359*, 300–313. [[CrossRef](#)]
22. Kiryukhantsev-Korneev, F.V.; Sytchenko, A.D.; Kudryashov, A.E.; Levashov, E.A.; Shtansky, D.V. The effect of Eu<sub>2</sub>O<sub>3</sub> additive to the TiCNiCr electrode on the formation of electrospark coatings. *Tech. Phys. Lett.* **2018**, *44*, 753–755. [[CrossRef](#)]
23. Kiryukhantsev-Korneev, P.V.; Sytchenko, A.D.; Kudryashov, A.E.; Levashov, E.A. Protective coatings produced by electro-spark deposition with TiCNiCr–(Eu<sub>2</sub>O<sub>3</sub>) electrodes. *CIS Iron Rev.* **2018**, *16*, 57–62. [[CrossRef](#)]
24. Sanchette, F.; Ducros, C.; Schmitt, T.; Steyer, P.; Billard, A. Nanostructured hard coatings deposited by cathodic arc deposition: From concepts to applications. *Surf. Coat. Technol.* **2011**, *205*, 5444–5453. [[CrossRef](#)]
25. Mattox, D.M. *The Foundations of Vacuum Coating Technology*, 2nd ed.; Elsevier/William Andrew: Norwich, NY, USA, 2018; p. 378.
26. Martin, P. Review of the filtered vacuum arc process and materials deposition. *Thin Films* **2001**, *394*, 1–14. [[CrossRef](#)]
27. Karlsson, L.; Hultman, L.; Johansson, M.; Sundgren, J.-E.; Ljungcrantz, H. Growth, microstructure, and mechanical properties of arc evaporated TiC<sub>x</sub>N<sub>1-x</sub> (0 ≤ x ≤ 1) films. *Surf. Coat. Technol.* **2000**, *126*, 1–14. [[CrossRef](#)]
28. Grimm, W.; Weihnacht, V. Properties of super-hard carbon films deposited by pulsed arc process. *Vacuum* **2010**, *85*, 506–509. [[CrossRef](#)]
29. Warcholinski, B.; Gilewicz, A.; Kuprin, A.; Tolmachova, G.; Ovcharenko, V.; Kuznetsova, T.; Zubar, T.; Khudoley, A.; Chizhik, S. Mechanical properties of Cr-O-N coatings deposited by cathodic arc evaporation. *Vacuum* **2018**, *156*, 97–107. [[CrossRef](#)]
30. Kiryukhantsev-Korneev, F.V.; Shirmanov, N.A.; Sheveiko, A.N.; Levashov, E.A.; Petrzhik, M.I.; Shtanskii, D.V. Nanostructural wear-resistant coatings produced on metal-cutting tools by electric-arc evaporation and magnetron sputtering. *Russ. Eng. Res.* **2010**, *30*, 910–920. [[CrossRef](#)]
31. Chang, C.-L.; Chen, Y.-W. Effect of the carbon content on the structure and mechanical properties of Ti–Si–C coatings by cathodic arc evaporation. *Surf. Coat. Technol.* **2010**, *205*, S1–S4. [[CrossRef](#)]
32. Johnson, L.; Rogström, L.; Johansson, M.; Odén, M.; Hultman, L. Microstructure evolution and age hardening in (Ti,Si)(C,N) thin films deposited by cathodic arc evaporation. *Thin Films* **2010**, *519*, 1397–1403. [[CrossRef](#)]
33. Lugscheider, E.; Knotek, O.; Zimmermann, H.; Hellmann, S. Investigation of the mechanical and structural properties of Ti–Hf–C–N arc PVD coatings. *Surf. Coat. Technol.* **1999**, *116*, 239–243. [[CrossRef](#)]
34. Kiryukhantsev-Korneev, P.V.; Sheveyko, A.N.; Kuptsov, K.A.; Novikov, A.V.; Shtansky, D. Ti–Cr–B–N coatings prepared by pulsed cathodic-arc evaporation of ceramic TiCrB target produced by SHS. *Prot. Met. Phys. Chem. Surfaces* **2013**, *49*, 677–681. [[CrossRef](#)]
35. Siemroth, P.; Schulke, T.; Witke, T. High-current arc—A new source for high-rate deposition. *Surf. Coat. Technol.* **1994**, *68*, 314–319. [[CrossRef](#)]
36. Engers, B.; Fuchs, H.; Schultz, J.; Hettkamp, E.; Mecke, H. Comparison of substrate temperature and deposition rate between modified pulsed arc process and d.c. arc process. *Surf. Coat. Technol.* **2000**, *133*, 121–125. [[CrossRef](#)]
37. Oliver, W.; Pharr, G. An improved technique for determining hardness and elastic modulus using load and displacement sensing indentation experiments. *J. Mater. Res.* **1992**, *7*, 1564–1583. [[CrossRef](#)]

38. Pierson, J.-F.; Billard, A.; Belmonte, T.; Michel, H.; Frantz, C. Influence of oxygen flow rate on the structural and mechanical properties of reactively magnetron sputter-deposited Zr–B–O coatings. *Thin Films* **1999**, *347*, 78–84. [[CrossRef](#)]
39. Lengauer, W. *Transition Metal Carbides, Nitrides, and Carbonitrides*; Wiley: Hoboken, NJ, USA, 2008; pp. 202–252. [[CrossRef](#)]
40. Furlan, A.; Lu, J.; Hultman, L.; Jansson, U. Control of crystallinity in sputtered Cr–Ti–C films. *Acta Mater.* **2013**, *61*, 6352–6361. [[CrossRef](#)]
41. Wdowik, U.; Twardowska, A.; Medala-Wasik, M. Lattice dynamics of binary and ternary phases in Ti–Si–C system: A combined Raman spectroscopy and density functional theory study. *Mater. Chem. Phys.* **2015**, *168*, 58–65. [[CrossRef](#)]
42. Escobar-Alarcón, L.; Medina, V.; Camps, E.; Romero, S.; Fernández, M.; Solís-Casados, D. Microstructural characterization of Ti–C–N thin films prepared by reactive crossed beam pulsed laser deposition. *Appl. Surf. Sci.* **2011**, *257*, 9033–9037. [[CrossRef](#)]
43. Bolelli, G.; Colella, A.; Lusvarghi, L.; Puddu, P.; Rigon, R.; Sassatelli, P.; Testa, V. Properties of HVOF-sprayed TiC–FeCrAl coatings. *Wear* **2019**, 36–51. [[CrossRef](#)]
44. Dilawar, N.; Mehrotra, S.; Varandani, D.; Kumaraswamy, B.; Haldar, S.; Bandyopadhyay, A. A Raman spectroscopic study of C-type rare earth sesquioxides. *Mater. Charact.* **2008**, *59*, 462–467. [[CrossRef](#)]
45. Zhang, G.; Gao, G.; Wang, X.; Lv, G.; Zhou, L.; Chen, H.; Pang, H.; Yang, S. Influence of pulsed substrate bias on the structure and properties of Ti–Al–N films deposited by cathodic vacuum arc. *Appl. Surf. Sci.* **2012**, *258*, 7274–7279. [[CrossRef](#)]
46. Fager, H.; Andersson, J.; Lu, J.; Jöesaar, M.J.; Odén, M.; Hultman, L. Growth of hard amorphous TiAlSiN thin films by cathodic arc evaporation. *Surf. Coat. Technol.* **2013**, *235*, 376–382. [[CrossRef](#)]
47. Glatz, S.; Koller, C.; Bolvardi, H.; Koložsvári, S.; Riedl, H.; Mayrhofer, P. Influence of Mo on the structure and the tribomechanical properties of arc evaporated Ti–Al–N. *Surf. Coat. Technol.* **2017**, *311*, 330–336. [[CrossRef](#)]
48. Chang, Y.-Y.; Yang, S.-J.; Wang, D.-Y. Characterization of TiCr(C,N)/amorphous carbon coatings synthesized by a cathodic arc deposition process. *Thin Films* **2007**, *515*, 4722–4726. [[CrossRef](#)]
49. Witke, T.; Schuelke, T.; Schultrich, B.; Siemroth, P.; Vetter, J. Comparison of filtered high-current pulsed arc deposition ( $\varphi$ -HCA) with conventional vacuum arc methods. *Surf. Coat. Technol.* **2000**, *126*, 81–88. [[CrossRef](#)]
50. Tsai, P.-C.; Chen, W.-J.; Chen, J.-H.; Chang, C.-L. Deposition and characterization of TiBCN films by cathodic arc plasma evaporation. *Thin Films* **2009**, *517*, 5044–5049. [[CrossRef](#)]
51. Eriksson, A.; Ghafoor, N.; Jensen, J.; Näslund, L.-Å.; Johansson, M.; Sjöln, J.; Odén, M.; Hultman, L.; Rosén, J. Arc deposition of Ti–Si–C–N thin films from binary and ternary cathodes—Comparing sources of C. *Surf. Coat. Technol.* **2012**, *213*, 145–154. [[CrossRef](#)]
52. Musil, J. Hard nanocomposite coatings: Thermal stability, oxidation resistance and toughness. *Surf. Coat. Technol.* **2012**, *207*, 50–65. [[CrossRef](#)]
53. Leyland, A.; Matthews, A. On the significance of the H/E ratio in wear control: A nanocomposite coating approach to optimised tribological behaviour. *Wear* **2000**, *246*, 1–11. [[CrossRef](#)]
54. Levashov, E.; Petrzhik, M.; Shtansky, D.; Kiryukhantsev-Korneev, P.; Sheveyko, A.; Valiev, R.; Gunderov, D.; Prokoshkin, S.; Korotitskiy, A.; Smolin, A.; et al. Nanostructured titanium alloys and multicomponent bioactive films: Mechanical behavior at indentation. *Mater. Sci. Eng. A* **2013**, *570*, 51–62. [[CrossRef](#)]
55. Martinez, D.M.; Cartes, C.L.; Justo, A.; Fernández, A.; Sanchez-Lopez, J.C. Self-lubricating Ti–C–N nanocomposite coatings prepared by double magnetron sputtering. *Solid State Sci.* **2009**, *11*, 660–670. [[CrossRef](#)]
56. Kuptsov, K.; Kiryukhantsev-Korneev, P.; Sheveyko, A.; Shtansky, D.; Shtansky, D. Comparative study of electrochemical and impact wear behavior of TiCN, TiSiCN, TiCrSiCN, and TiAlSiCN coatings. *Surf. Coat. Technol.* **2013**, *216*, 273–281. [[CrossRef](#)]
57. Zhang, L.; Ma, G.; Ma, H.; Lin, G. Effect of pulsed bias voltage on the structure and mechanical properties of Ti–C–N composite films by pulsed bias arc ion plating. *Nucl. Instrum. Methods Phys. Res. Sect. B Beam Interact. Mater. Atoms* **2014**, *333*, 1–5. [[CrossRef](#)]
58. Chen, R.; Tu, J.; Liu, D.; Mai, Y.; Gu, C. Microstructure, mechanical and tribological properties of TiCN nanocomposite films deposited by DC magnetron sputtering. *Surf. Coat. Technol.* **2011**, *205*, 5228–5234. [[CrossRef](#)]

59. Zhang, F.; He, J.; Chen, K.; Qin, Y.; Li, C.; Yin, F. Microstructure evolution and mechanical properties of TiCN–Cr nano/micro composite coatings prepared by reactive plasma spraying. *Appl. Surf. Sci.* **2018**, *427*, 905–914. [[CrossRef](#)]



© 2019 by the authors. Licensee MDPI, Basel, Switzerland. This article is an open access article distributed under the terms and conditions of the Creative Commons Attribution (CC BY) license (<http://creativecommons.org/licenses/by/4.0/>).